

Spray-Dried Mesoporous Mixed Cu-Ni Oxide@Graphene Nanocomposite Microspheres for High Power and Durable Li-Ion Battery Anodes


Louis Lefrançois Perreault, Francesca Colò, Giuseppina Meligrana, Kyoungsoo Kim, Sonia Fiorilli, Federico Bella, Jijeesh R. Nair, Chiara Vitale-Brovarone, Justyna Florek, Freddy Kleitz,* and Claudio Gerbaldi*

Exfoliated graphene-wrapped mesoporous Cu-Ni oxide (CNO) nanocast composites are developed using a straightforward nanostructure engineering strategy. The synergistic effect of hierarchical mesoporous CNO nanobuilding blocks that are homogeneously wrapped by graphene nanosheets (GNSs) using a rapid spray drying technique effectively preserves the electroactive species against the volume changes resulting from the charge/discharge process. Owing to the intriguing structural/morphological features arising from the caging effect of exfoliated graphene sheets, these 3D/2D CNO@GNS nanocomposite microspheres are promising as high-performance Li-ion battery anode materials. They exhibit unprecedented electrochemical behavior, such as high reversible specific capacity (initial discharge capacities exceeding 1700 mAh g^{-1} at low 0.1 mA g^{-1} , stable 850 and 730 mAh g^{-1} at 1 and 5 mA g^{-1} after 800 and 1300 cycles, respectively, and higher than 400 mAh g^{-1} at very high current density of 10 mA g^{-1} after more than 2000 cycles), excellent coulombic efficiency and long-term stability (more than 3000 cycles with >55% capacity retention) at high current density that are remarkable compared to most transition metal oxides and nanocomposites prepared by conventional techniques. This simple, yet innovative, material design is inspiring to develop advanced conversion materials for Li-ion batteries or other energy storage devices.

1. Introduction

The secondary lithium ion battery (LiB) is considered as one of the most promising ways to store energy owing to a number of outstanding features, such as high energy density, elevated operating potential, extended cycle life, no memory effect, and environmental friendliness.^[1] This type of battery permitted the revolution of portable electronic devices in the 90s and, today, it is the dominant source of power for smart mobile devices, laptops, cameras, etc.^[2] With an international market value that exceeds over 30 billion US dollars,^[3] research and development on LiBs is still very much active. The ever-growing LiB technology further targets the emerging applications in bigger-scale devices for the reversible storage of large amounts of energy.^[4] Indeed, present environmental crisis calls for a global change and considering the great environmental benefit, highly efficient electric or hybrid-electric

L. Lefrançois Perreault
Department of Chemistry
Université Laval
Quebec City G1V 0A6, QC, Canada
Dr. F. Colò, Dr. G. Meligrana, Dr. F. Bella, Dr. J. R. Nair,
Prof. C. Gerbaldi
GAME Lab
Department of Applied Science and Technology – DISAT
Politecnico di Torino
Corso Duca degli Abruzzi 24, 10129 Turin, Italy
E-mail: claudio.gerbaldi@polito.it

 The ORCID identification number(s) for the author(s) of this article can be found under <https://doi.org/10.1002/aenm.201802438>.

© 2018 The Authors. Published by WILEY-VCH Verlag GmbH & Co. KGaA, Weinheim. This is an open access article under the terms of the Creative Commons Attribution-NonCommercial License, which permits use, distribution and reproduction in any medium, provided the original work is properly cited and is not used for commercial purposes.

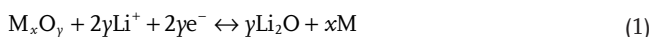
DOI: 10.1002/aenm.201802438

Dr. K. Kim
Center for Nanomaterials and Chemical Reactions
Institute for Basic Science (IBS)
Daejeon 305-701, Republic of Korea
Prof. S. Fiorilli, Prof. C. Vitale-Brovarone
IRIS
SIMTI Group
Department of Applied Science and Technology – DISAT
Politecnico di Torino
Corso Duca degli Abruzzi 24, 10129 Turin, Italy
Dr. J. Florek, Prof. F. Kleitz
Department of Inorganic Chemistry – Functional Materials
Faculty of Chemistry
University of Vienna
Währinger Straße 42, 1090 Vienna, Austria
E-mail: freddy.kleitz@univie.ac.at

vehicles (EVs/HEVs) are expected to play a crucial role in the reduction of greenhouse gases and urban pollution.^[5] Unfortunately, LiBs almost reached the maximum obtainable performance with the current design and the active materials used in the electrodes, which is one of the most severe drawbacks for their widespread inclusion in EVs/HEVs.^[6–8]

As per the present design, on the anode side the rather slow diffusivity of lithium ions within the stacked graphene layers of graphite might be improved to achieve the demanding high-power levels requested by the next-generation, high-performing storage systems in order to be effectively used in bigger systems, such as cars or buses.^[9] Limitations can be overcome by developing innovative electrode designs and architectures and the proper heat management of the cells. Satisfying all the requirements to replace conventional graphite-based anodes is an enormous task, nevertheless several new materials have been explored and research continues to be very much focused on this objective.^[10] In this respect, nanostructured materials (including nanoparticles, nanowires, nanosheets, and nanoporous structures) exhibiting high surface area, large reversible storage capacity, and relatively high operating potential that ensure enhanced safety have been investigated over the past years.^[6,8,11–16]

Since their introduction by Tarascon and co-workers in 2000,^[6] transition metal oxide-based (TMO, where M = Co, Ni, Cu, Fe) systems showing practical reversible specific capacity up to 700 mAh g⁻¹ and good capacity retention upon cycling have been viewed as a promising alternative to carbon-based anodes (practical capacity ≤350 mAh g⁻¹), and are being intensively pursued by the scientific community.^[17,18] Here, unlike carbon-based anodes, TMOs undergo a conversion process for alkali metal ion storage that follows this equation^[6,8,19,20]



In this case, the specific capacity is determined by the accessibility of the active sites of the active material particles in the electrode. The number of active sites can be increased by designing materials having large specific surface area and open structures with high degree of porosity.^[11,13,21] In this respect, the nanocasting technique is a simple and easy way to produce robust mesoporous metal oxides or mixed metal oxides with large surface-to-volume ratio.^[22–27] Using this technique, for instance, nanoscale mixed Cu-Fe oxide was synthesized and tested as active material in Li-ion cells.^[28] Even though, these mixed oxides had shown promising results as lithium battery anode, the charge/discharge stability upon prolonged cycling remained limited.^[6–8,19,13,29,30] Indeed, the issue of stability and performance of TMOs is originating from the dramatic volume change upon reversible storage of Li⁺ ions in the active material particles, which leads to the destruction of original structure during charge/discharge cycling. Specific pore designing strategies have been employed to diminish this effect in TMOs, such as adding an empty buffer in the material. It resulted in the development of mesoporous TMOs with crystalline walls that combine nanosized pores for facile diffusion of lithium ions with sub-micrometric particle sizes ensuring an intimate interparticle connection.^[28,31,32] However, even with a mesoporous 3D structure, achieving the long-term cycling stability

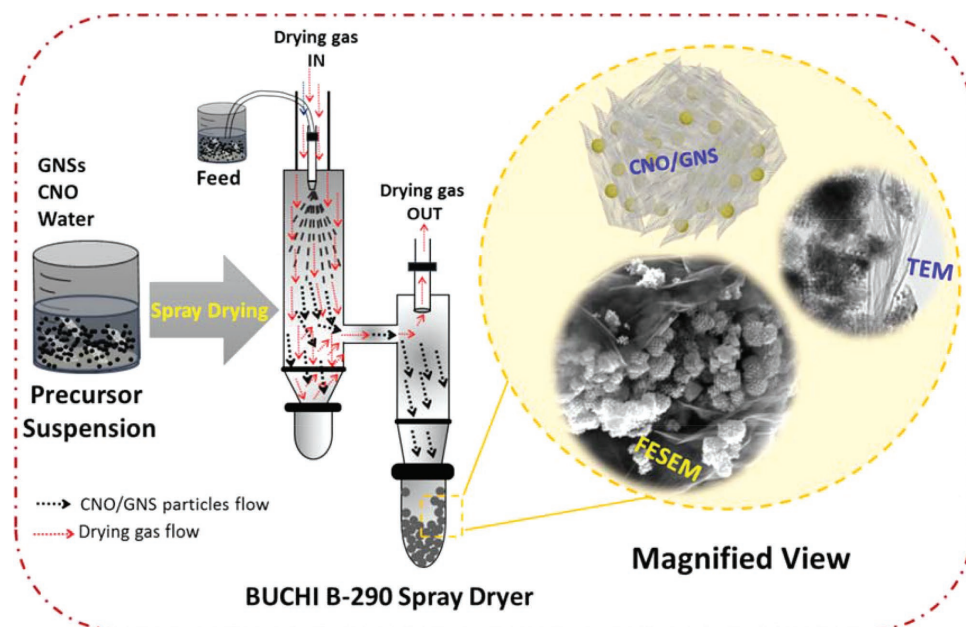
(>100 cycles at 100% depth of discharge (DoD)) remains a challenge as it fails to meet both the energy and the power demand for real practical application of any industrial value.^[33,34]

In order to increase the electrochemical performance and the long-term stability of TMO-based electrodes, various techniques have been employed, for example, the preparation of hybrid structures with carbon and related materials.^[12,20,21,35–37] These hybrid materials are interesting as the carbonaceous materials impart high electrical conductivity and fair ductility that contribute in mitigating the TMOs negative features, such as low electrical conductivity, easy agglomeration, and dramatic volume change during cycling.^[29] As carbonaceous structure, graphene nanosheets (GNSs) exhibit many intriguing and unconventional properties: genuine electron transport, peculiar surface properties, enhanced thermal stability, and outstanding mechanical robustness despite being the thinnest known materials, which are made of a flat monolayer of carbon atoms tightly arranged in a 2D honeycomb structure. As a result, GNSs hold promising characteristics as an excellent additive for the preparation of this kind of hybrid materials.^[38,39] Nevertheless, the development of a simple route to achieve controlled architecture at the nanoscale with enhanced electronic conductivity and high energy density for long-term cycling remains an open challenge. In this respect, we report here an effective spray drying technique for the preparation of a composite material combining mesoporous mixed CuO-NiO (CNO) particles enwrapped within exfoliated graphene nanosheets. 3D porous microspheres are obtained, in which the mesoporous CNO nanoblocks are wrapped by GNSs and confined within a continuous conductive network. Compared to existing approaches, the proposed engineering strategy is facile and efficient; it is a water-based process, thus environmentally benign and ready to be scaled up at an industrial level.

2. Results and Discussion

The summary for the preparation procedure of the CNO@GNS nanocomposite microsphere active material is shown in **Scheme 1**. A selected amount (generally ≤500 mg) of hierarchical mesoporous binary CNO particles, which were obtained by nanocasting,^[19,20] was added to a water suspension of GNSs (with a final CNO:GNS weight ratio of 15:1), and the resulting mixture sonicated and, then, spray-dried to form the 3D/2D CNO@GNS nanocomposite microspheres. In this procedure, the mixture is pumped into a spray drying apparatus using a peristaltic pump and nebulized through a nozzle by a heated gas carrier to form aerosol droplets, which are subsequently dried in the cylinder, as illustrated in Scheme 1. The droplets of suspension containing CNO nanoparticles and GNSs, upon drying in the combined spray/cyclone step, produced the nanocomposite CNO@GNS 3D/2D microaggregates, in which the CNO nanocast particles were uniformly distributed among the graphene sheets. During this process, the mixed oxide nanoparticles were anchored uniformly on the surface of the GNSs, which can tightly wrap on the surface of CNO by electrostatic interactions, as clearly seen in the magnified view on the right-hand side of Scheme 1.

First, the crystal structure of the as-prepared CNO@GNS nanocomposite microspheres was verified by powder X-ray



Scheme 1. Schematic representation of the procedure to synthesize the 3D/2D nanocomposite microsphere CNO@GNS active electrode material through spray drying.

diffraction (XRD) analysis. The corresponding patterns are shown in **Figure 1** and Figure S1 (Supporting Information). For comparison, the XRD pattern of the pure nanocast mesoporous CNO nanostructure is also shown. The wide-angle XRD pattern of the as-prepared nanocast CNO before combination with graphene (curve (a)) shows the characteristic reflection peaks of the NiO phase at 37.20° and 43.32° . The other less intense components at 35.58° and 38.78° are due to the reflection peaks of the CuO phase. The calculated ratio intensities of the peaks due to NiO and CuO phases were found to be higher than the nominal value in the starting mixture (CuO/NiO = 0.5). This finding is in good agreement with XRD results reported by

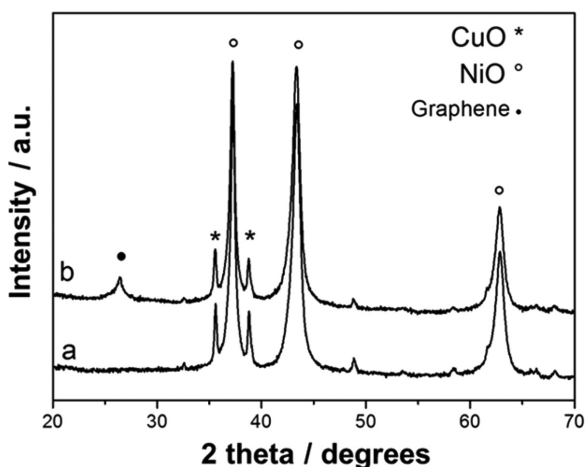


Figure 1. Powder X-ray diffraction patterns (PXRD) of a) pristine nanocast mesoporous CNO particles and b) CNO@GNS nanocomposite microspheres. For clarity, only the main diffraction peaks of the CuO phase are highlighted with symbols, other visible peaks with low intensity are assigned to the same monoclinic CuO phase.

Yen and Kleitz^[22] related to bi-component CuO-NiO nanocast products prepared with a comparable CuO:NiO molar ratio of 1:3, the diffractograms of which consist mainly of peaks associated with the NiO cubic rock-salt phase, indicating that CuO is soluble in NiO and forms a cubic rock-salt solid solution, with a general formula corresponding to $\text{Cu}_x\text{Ni}_y\text{O}$. The latter appears as the main phase and a fraction of CuO is observed as a segregated phase. Higher Cu content (e.g., CuO/NiO = 1) leads to the undesired much more pronounced occurrence of the CuO phase (Figure S1b, Supporting Information).^[13] In the next step, the diffractogram obtained for the spray-dried CNO@GNS 3D/2D nanocomposite (Figure 1b) reveals, as expected, reflection peaks originating from the mixed oxide powder and the appearance of a second component at around 26.5° , easily assigned to GNSs. The relatively low intensity of the diffraction peak is most likely attributed to the ultrathin characteristics of the graphene sheets, which do not include noticeable amount of stacked crystalline lamellar graphitic phases; this is well in agreement with similar results already reported in the literature for other GNS-wrapped TMOs.^[40,41] No other obvious peaks are detected, accounting for the stability of the nanocast CNO particles, which did not experience noticeable modifications upon spray drying and following heat treatment. Furthermore, the low angle XRD pattern of the mesoporous CuO-NiO (Figure S1, Supporting Information), which was prepared using 3D cubic KIT-6 silica as the template, shows weak diffraction peaks at low 2-theta values that can be associated to the mesoscopic structure of the CNO nanocast, suggesting adequate replication of the silica mesostructure, in agreement with previous reports.^[22,42]

The morphological characteristics of the spray-dried hybrid CNO@GNS 3D/2D nanocomposite microspheres, as revealed by scanning and transmission electron microscopies, are shown in **Figures 2** and **3**, respectively. High resolution scanning electron

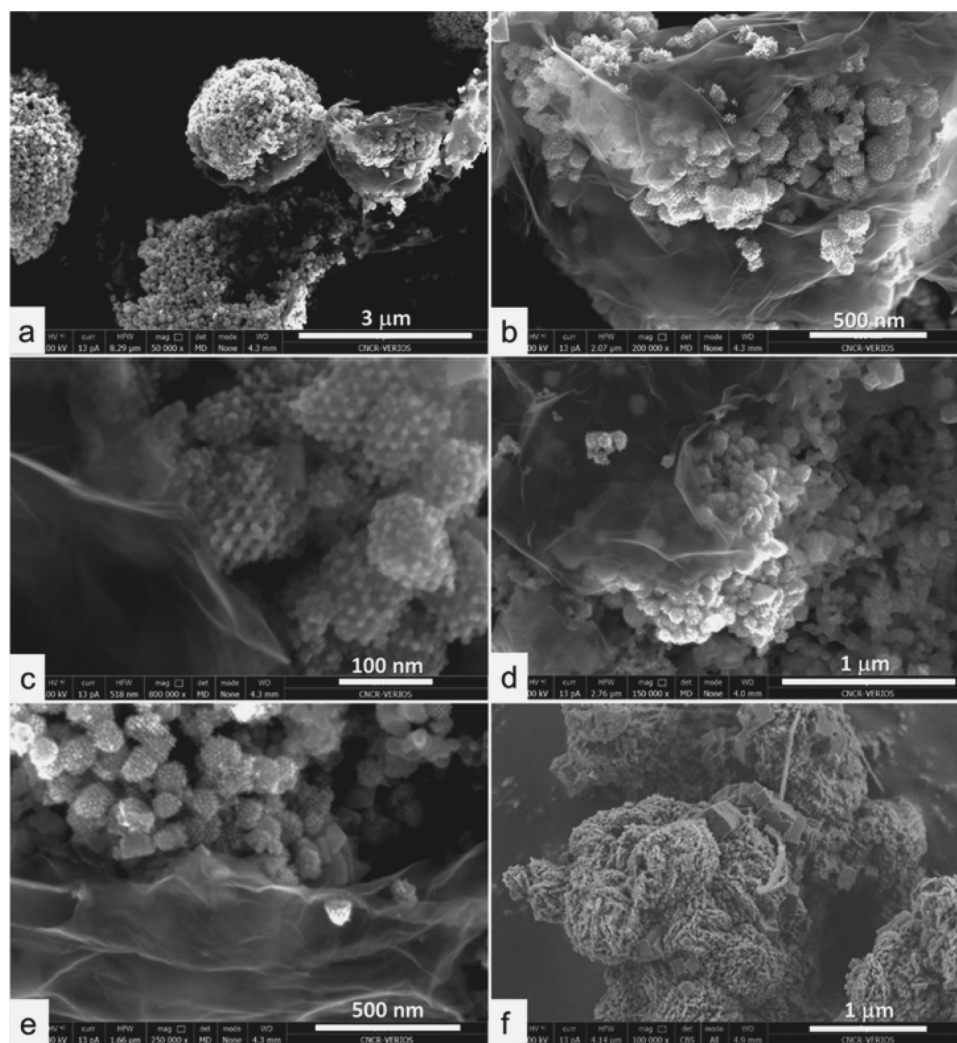


Figure 2. HRSEM images of a–c) as-prepared 3D/2D CuO-NiO@graphene nanocomposite microsphere active material powder and CuO-NiO@graphene-based electrode material d,e) before cycling and f) after cycling.

microscopy (HRSEM) images (Figure 2a,b) show that the composite clearly consists of relatively uniform micrometersized spheroidal aggregates of 3D mixed CuO-NiO nanoparticles and homogeneously intercalated 2D graphene nanosheets with an average diameter in the range of 2.5 μm . This observation suggests that the spray drying process, combined with an ultrasonication treatment of the powder suspension, is an effective one-step route to produce a composite system where nanosized polyhedrons of mixed CNO are tightly wrapped with GNSs. Furthermore, the magnified SEM images (Figure 2b,c) definitely enlighten that the microspheres are actually composed of extended interconnected layers of graphene that enfold and accommodate a large number of mesoporous polyhedrons, with abundant space and voids between them. This is beneficial for electrolyte infiltration, thus optimum wetting of the active material particles; moreover, the interconnected 3D/2D structures should allow for fast ion transport and electronic kinetics, which in turn should account for an improved stability of the resulting nanocomposites versus prolonged cycling in real cell configuration (*vide infra*). Figure 2d,e shows that this

arrangement is preserved once the composite electrode film is prepared with this nanocomposite powder (the carboxymethylcellulose (CMC) and Super-P, as binding and electronic conductivity enhancer materials, respectively, are clearly visible connecting and contacting the active material particles). Detailed nanostructures and morphologies after the wrapping procedure were further investigated by transmission electron microscopy (TEM), and the results are shown in Figure 3. The ordered mesoporous structure of the nanocast CNO replicated from mesoporous KIT-6 silica was also evidenced by the TEM observations. The images further confirm the elevated porosity of the assembled 3D/2D composite, which are actually constructed from numerous interconnected nanosized CNO polyhedrons of 50–100 nm in size, effectively and intimately enwrapped and interconnected by the GNS network. The network of graphene sheets can be roughly estimated as composed of stacking of multiple single graphene layers, which are easily distinguished in the micrographs (Figure 3a,b). As can be furthermore noticed, extended domains of ordered 3D mesoporous structures of the mixed-oxide replicas are clearly

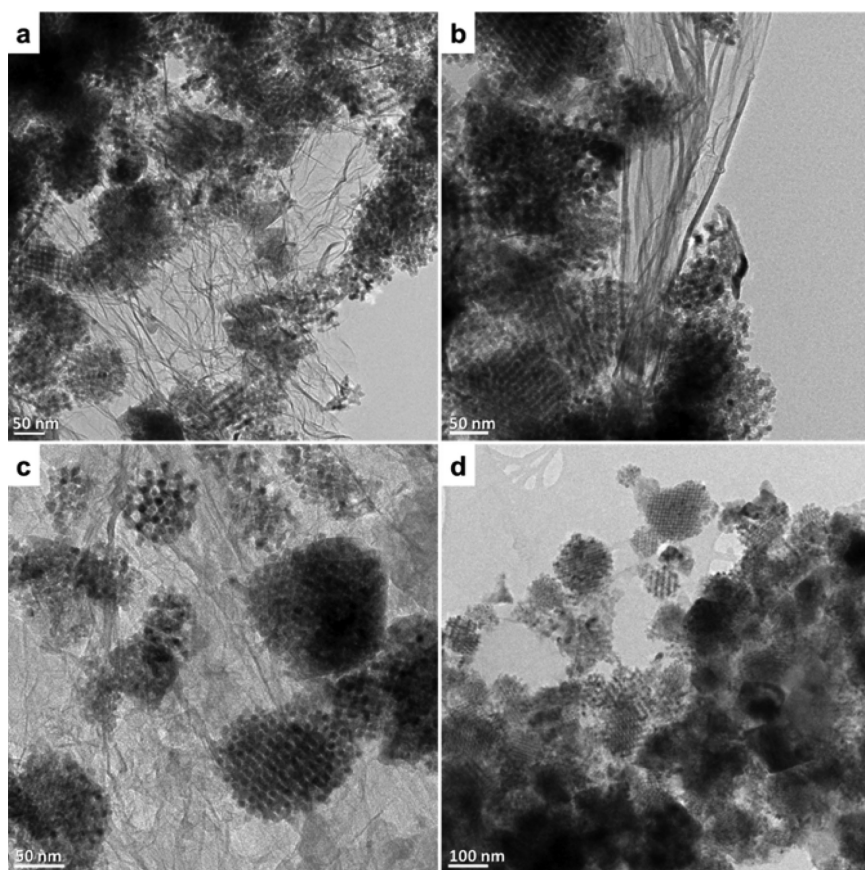


Figure 3. TEM images of a,b) as-prepared CuO-NiO@graphene nanocomposite microspheres active material powder and CuO-NiO@graphene-based electrode material c) before cycling and d) after cycling.

evidenced, which have preserved their morphologies even after the thermal treatment in inert atmosphere without undergoing any significant agglomeration, and appearing tightly anchored to the GNS network.^[43] Figure 3c confirms that this GNS/CNO arrangement is preserved once the composite electrode film has been prepared.

The well-defined CNO nanoparticles tightly wrapped into graphene sheets imply that the composite also retains a high surface area. In this respect, the porous features of the materials were confirmed by nitrogen isothermal adsorption/desorption measurement. First, the N_2 adsorption–desorption isotherm at $-196\text{ }^\circ\text{C}$ of the initial CuO-NiO and the corresponding pore size distribution are shown in Figure S2 (Supporting Information). In terms of porosity, the nanocast samples showed high nitrogen sorption capacity with an isotherm being characteristic of well-developed mesoporous nanocast metal oxides.^[44,45] The sample shows high specific Brunauer–Emmett–Teller (BET) surface area and high pore volume, respectively, $93\text{ m}^2\text{ g}^{-1}$ and $0.17\text{ cm}^3\text{ g}^{-1}$, which are comparable to values reported for nanostructured mixed metal-oxide obtained by the nanocasting pathway.^[13,22] The pore size distribution (shown in the inset of Figure S2, Supporting Information), calculated using nonlocal density functional theory (NLDFT) method, evidences a main component centered at around 4.4 nm, attributed to mesoporous channels resulting from the replication of the silica template, and a

second much wider distribution, possibly due to the interparticle voids.

The chemical features, composition, and surface electronic state of the mixed CuO-NiO were investigated by energy-dispersive spectroscopy (EDS) and X-ray photoelectron spectroscopy (XPS) measurements (see Figure S3, Supporting Information). The Ni/Cu ratio obtained by EDS is 2.36, which gives chemical composition on larger scale, and it is very close to the synthesis nominal ratio (Ni/Cu = 2.00). In contrast, the chemical ratio in the near-surface region obtained from the XPS analysis is 3.6, higher than the nominal, suggesting an enrichment of NiO phase at the grain surface, in line with our previous observations concerning this type of structure.^[22]

Convinced by the beneficial influence of their peculiar structural/morphological characteristics, the newly elaborated CNO@GNS 3D/2D nanocomposite microspheres were subjected to thorough electrochemical characterization by means of both cyclic voltammetry (CV) and long-term constant current (galvanostatic) discharge/charge cycling, in lab-scale electrochemical test cells using standard liquid electrolyte and metallic lithium as both the counter and the reference electrodes. Advantages of the new 3D/2D configuration are highlighted by comparison with the lithium storage performance of the

bare hierarchical mesoporous CNO nanocasts under the same electrochemical conditions.

Figure 4 shows the typical cyclic voltammetric profiles of (a) the CNO@GNS 3D/2D nanocomposite microspheres (initial ten cycles) and (b) CNO nanocast (initial five cycles) electrodes at a scan rate of 0.1 mV s^{-1} in the potential scan range between 0.01 and 3 V versus Li^+/Li . Clearly, the initial scan toward anodic potential values is dominated by the large reduction peak (assigned as S) centered at around 0.9 V with a shoulder at $\approx 1.07\text{ V}$ versus Li^+/Li assigned as 1. As for its evident disappearance in the following scans, the intense peak S may be ascribed to the formation of the solid electrolyte interphase (SEI) layer, resulting from the irreversible reduction of some of the electrolyte components (mainly solvents, although other electrolyte components such as salts may contribute to formation of specific products) at the surface of the anode active material particles, typically experienced below 1 V versus Li^+/Li .^[6,11,46] As for this attribution, the shoulder 1 may be assigned to the onset of the NiO and CuO reduction, associated with the decomposition of the mixed oxide into metallic Ni and Cu with the formation of Li_2O , which overlaps with the SEI formation process. Indeed, during the second cathodic scan, only a clear reduction process is observable at about 1.1 V versus Li^+/Li , the position of which slightly shifts toward lower potential values, thereby evidencing that the oxide microstructures underwent

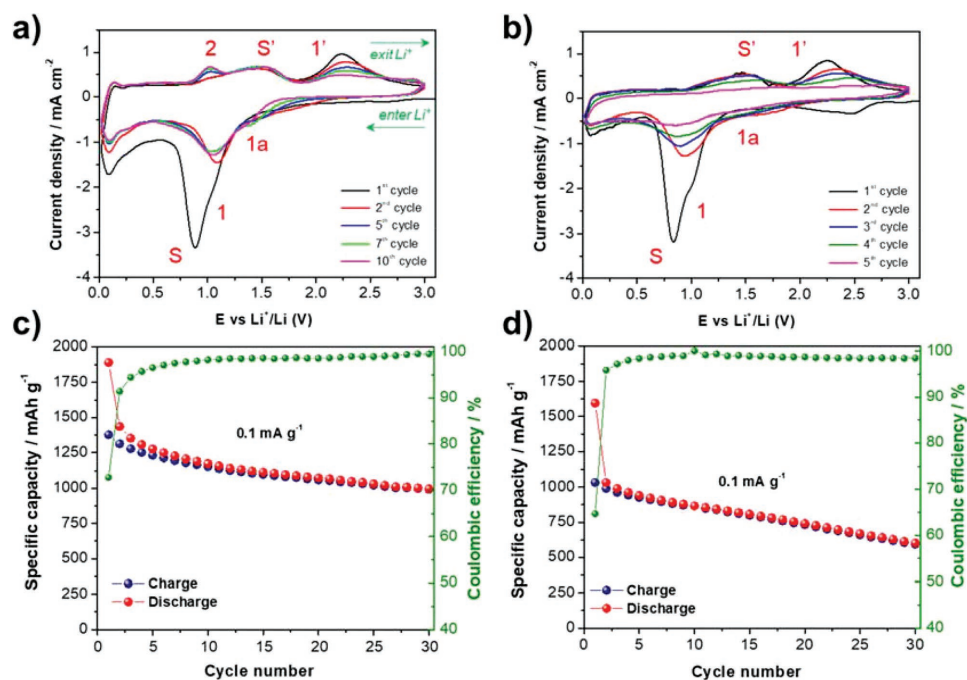


Figure 4. Comparison of the ambient temperature electrochemical behavior of the samples under study: a,b) cyclic voltammetry (scan rate of 0.1 mV s^{-1}) of CNO@GNS nanocomposite microspheres and CNO nanoparticle electrodes, respectively; c,d) constant-current (galvanostatic) charge/discharge cycling behavior (initial 30 cycles at 0.1 mA g^{-1}) and the corresponding coulombic efficiency (%) of CNO@GNS nanocomposite microspheres and CNO nanoparticle electrodes, respectively.

significant modifications upon reversible reaction with lithium ions in the course of the first CV cycle. In the subsequent cycles, the shape and position of the reduction peak change to a lesser extent, in fact stabilizing at about 1.03 V versus Li^+/Li , which accounts for a fair reversibility of the electrochemical phenomenon in the 3D/2D nanocomposite. Upon cycling, a second less intense reduction peak appears toward more anodic potential values (assigned as 1a). In agreement with previous reports,^[47–49] it can be attributed to the lithium insertion into CuO , which typically occurs at slightly higher potential with respect to NiO , and matches with the relative composition of the two oxides in the material as calculated by XPS/EDS. These results are consistent with previous literature reports.^[50,51] Some redox processes at potential values below 0.3 V versus Li^+/Li are observed, along with an increased overpotential between cathodic and anodic profiles, which more likely account for the reversible storage of lithium ions into graphene sheets mainly due to some capacitive effects. During the following anodic scan, we may observe two dominant oxidation phenomena, which develop into two rather broad peaks at around 1.5 and 2.3 V versus Li^+/Li . The first peak, assigned as S' , is associated with the partial decomposition of the SEI layer, while the main oxidation peak that develops at 2.3 V , assigned as $1'$, accounts for the oxidation reactions of Ni and Cu into the corresponding oxides (mainly superimposed, as they typically develop within very similar potential range) associated with the lithium extraction process, based on the following reactions^[52,53]:



A specific feature of the CNO@GNS nanocomposite electrode is the presence of the anodic peak assigned as 2 in Figure 4a, which develops at about 1.03 V versus Li^+/Li after some consecutive cycles and increases in its intensity upon cycling. Indeed, this behavior represents a somewhat puzzling feature, but we might reasonably presume that it arises from some reversible faradaic processes involving the CNO redox system and is favored by the presence of the electronically conducting graphene sheets. The apparently unusual position of the peaks (the corresponding reduction is evident as a shoulder of the 1 peak appearing below 0.8 V versus Li^+/Li during the fifth cycle) at very cathodic potentials may be related to the presence of metal and/or oxide particles having a rather broad size distribution in the nanorange, which results in a sizeable shift of oxidation/reduction potentials, in agreement with the studies on nanosized copper oxide systems by Valvo et al.^[11] Notably, the CNO@GNS nanocomposite microsphere electrode was able to withstand ten complete CV cycles without losing its electrochemical characteristics; indeed, most of the reduction/oxidation peaks are still clearly observable, only slightly reduced in their intensity, with peak positions almost unchanged. This is an indication of improved stability of the 3D/2D nanocomposite if compared to the CNO nanocast electrode, the profile of which after only five cycles already lost most of its specific features both at higher and lower potentials, in turn indicating severe modifications of the active particles structure with detrimental consequences on the overall electrode integrity and more reversible capacity losses. The enhanced CV features in terms of stability and reversibility of the CNO@GNS 3D/2D nanocomposite are easily ascribable to the presence of graphene sheets in the hybrid composite.

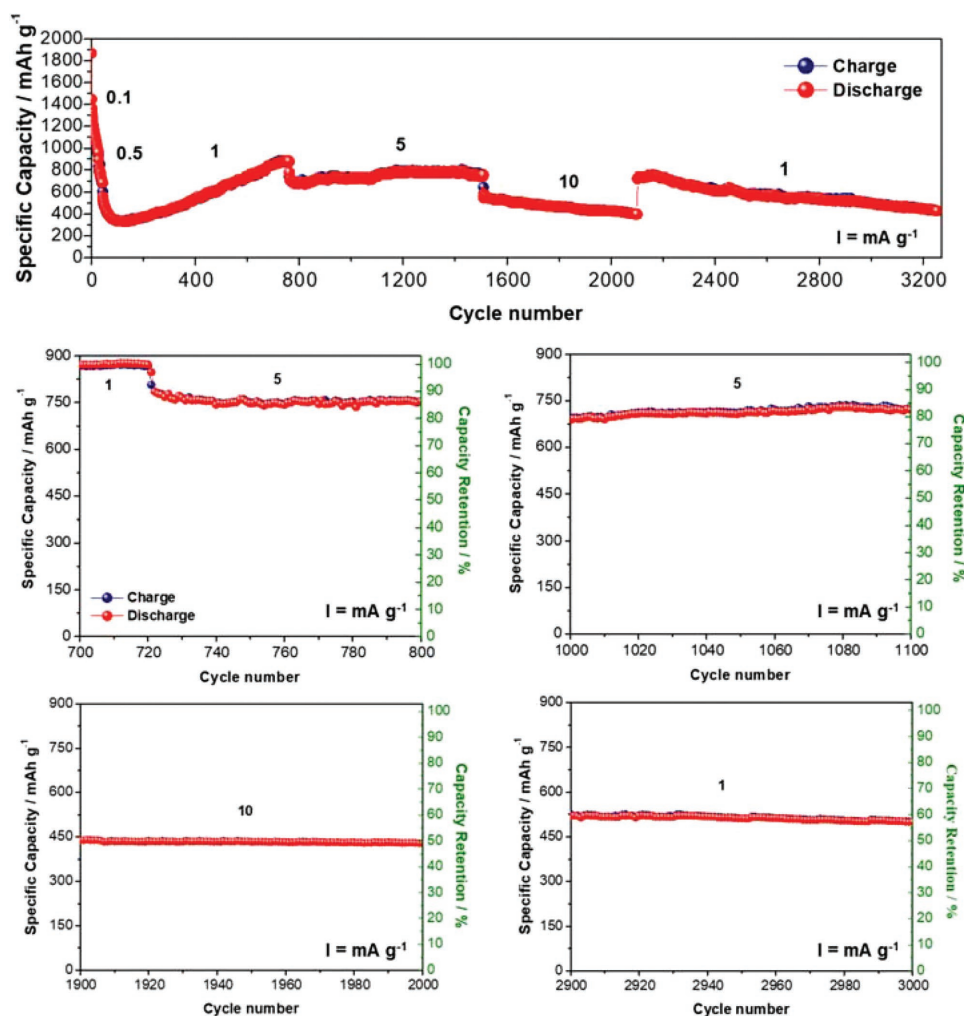


Figure 5. Ambient temperature very long-term (>3000 reversible charge/discharge cycles) constant-current cycling at different current densities (0.1–10 mA g⁻¹) for the CNO@GNS nanocomposite microsphere electrode in lab-scale lithium cell. All current density values (*I*) are given in mA g⁻¹.

Overall, the highly conductive GNSs ensure a better electrical contact between particles as well as with the current collector, thus enhancing kinetics, lithium ion transfer, and extent of electrode reactions. Moreover, the separation between cathodic (1) and anodic 1' peaks is clearly narrower if compared to the bare CNO nanocast electrode, which indicates reduced polarization and improved reversibility for the composite with GNSs. The comparison of the constant-current (galvanostatic) charge/discharge cycling behavior is shown in Figure 4, where the initial 30 cycles at 0.1 mA g⁻¹ are presented for (c) CNO@GNS nanocomposite microsphere and (d) CNO nanoparticle electrodes. It clearly underlines the remarkably enhanced reversible storage capability of the graphene-enwrapped sample, which demonstrated an almost 30% increase in specific capacity upon initial cycling at low current density and even higher capacity retention if compared to the bare one (i.e., 72% vs 57%, respectively). Clearly, the very high surface area of the electrode material is not a favorable characteristic as it increases the decomposition of the electrolyte components, which may lead to thicker SEI formation. Nonetheless, the positive features of our proposed engineering strategy are

also reflected on the initial cycling behavior, where the wrapped graphene-based mixed metal oxides showed higher coulombic efficiency than the sample without the graphene wrapping (i.e., 73% vs 64%, respectively). However, the initial capacity decay must be properly resolved through further investigations in order to achieve practical initial efficiency.

The CNO@GNS nanocomposite microsphere electrode was then subjected to prolonged ambient temperature constant-current (galvanostatic) cycling to understand the capability of the material to store lithium ions during charge and extract them during discharge in a highly reversible manner. As shown in **Figure 5**, cycling studies were also performed for more than 3000 cycles at different current densities from 0.1 to 10 mA g⁻¹ (these correspond to 12.8 and 1280 mA for the effective electrode areal active material loading of about 7.8 mg) and achieved a stable cycling throughout the full testing with some peculiar characteristics, which are thoroughly explained below.

Figure 6a–c shows the constant-current cycling response of the CNO@GNS nanocomposite microsphere electrode in lithium cell for 500 cycles at high 1 mA g⁻¹ (plot (c)), along with the potential versus specific capacity profiles at different

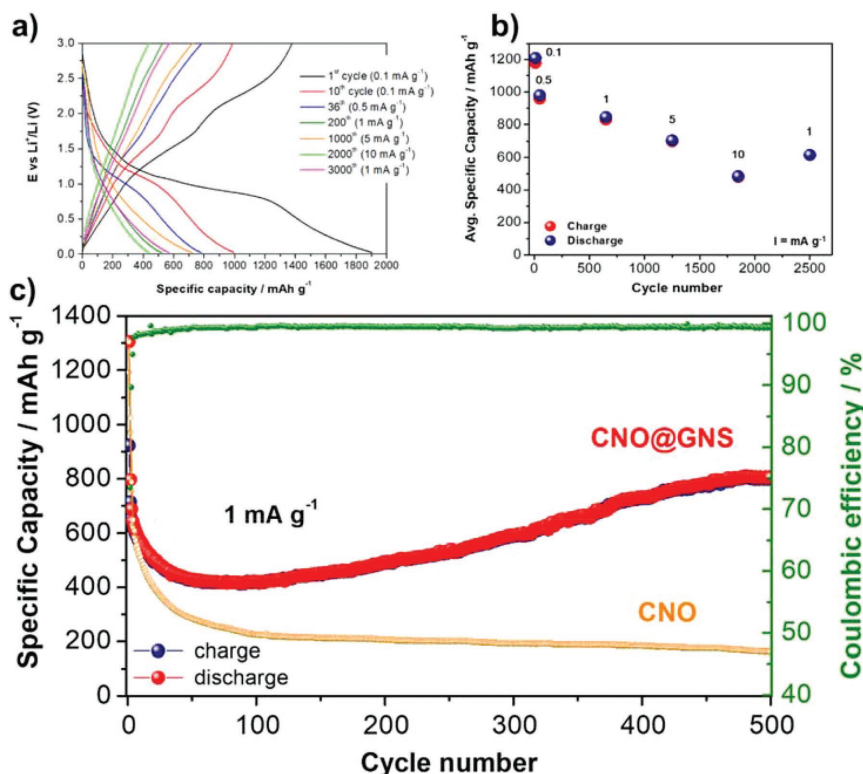


Figure 6. Ambient temperature constant-current (galvanostatic) charge/discharge cycling behavior of the 3D/2D CNO@GNS nanocomposite microsphere electrode: a) potential versus specific capacity profiles and b) rate capability plot at different current densities and cycle number, and c) specific capacity and coulombic efficiency versus cycle number (500 cycles at 1 mA g⁻¹) compared to the bare CNO electrode. All current density values (I) are given in mA g⁻¹.

current densities (plot (a)) and the rate capability (plot (b)). It delivers a specific capacity of about 1305 mAh g⁻¹ upon first discharge (Li⁺ ions insertion) and about 900 mAh g⁻¹ upon first charge, which corresponds to a low initial coulombic efficiency around 70%, as previously discussed. However, already in few cycles the electrode stabilizes its behavior, attaining a coulombic efficiency exceeding 99% at the fifth cycle, which then remains very stable for the whole test. The irreversible loss is pertaining to many factors such as: i) extended SEI layer formation due to the high surface area (see also results from CV) and ii) presence of graphene nanosheets that can react in the early stages with the electrolyte, thus resulting in increased active surface area exposed to redox processes. After the initial induction cycles, the cell provides very high efficiency values. The positive characteristics in terms of high coulombic efficiency after initial cycling account for the high reversibility of the electrochemical process in the electrode material as well as the overall structural stability of the active material particles upon reversible cycling. A remarkable integrity of the formed SEI layer is also envisaged and this is clearly ascribed to the GNS wrapping that may buffer the severe volume changes typical of CNO nanostructures, thus limiting to a great extent the fracturing, and resulting recursive formation, of the formed SEI layer onto the active material particles. In the same testing condition, the bare CNO electrode shows similar initial specific capacity values, followed by a monotonous rapid decrease of

performance, which resulted in specific capacity values approaching 150 mAh g⁻¹ after 500 cycles.

On the contrary, a peculiar feature of the CNO@GNS nanocomposite microsphere electrode is the rapid decay of specific capacity in the initial stages followed by a continuously increasing electrochemical performance to reach a steady value of about 800 mAh g⁻¹ after 500 cycles. Such a phenomenon was observed in similar systems where porous nanostructured (mixed) metal oxides were employed.^[43,47] According to previously reported results by Guo et al.,^[47] such materials undergo an activation process in the initial stages, where slowly an increasing portion of the material is activated at the electrochemical reaction. The electrolyte wettability to the active sites, disintegration and integration of nanoparticles and agglomerates thereof during cycling to reach a stable phase, with facilitated lithium diffusion, and more active sites for lithium ion storage, are some of the suggested reasons for such a phenomenon. In our present case, a considerably longer activation process is required and the cell reaches a steady behavior only after a sizeable number of cycles, which was never reported in the literature so far. We may relate this to the presence of the graphene sheets, which behave as an efficient elec-

tronic conductive substrate even when added in relatively low amount. If such an anode is used in a full cell, in our opinion, during the long-term cycling stages, the anode can act as a reservoir to compensate the loss of Li⁺ ions, which arises from the continuous degradation process occurring at the cathodic side due to the formation of interphase passivation layers. How much of this hypothesis can be realized is a difficult question to address at this moment. Nevertheless, future efforts are necessary to reduce the initial capacity loss so that a more stable specific capacity trend is achieved.

Overall, the stability of the newly developed composite electrode material is remarkable: the CNO@GNS-based cell demonstrated excellent cyclability and relatively satisfying specific capacity even at high current regimes. Indeed, the cell was charged and discharged at different scan rates between 0.1 and 10 mA g⁻¹ (see also Figure 5). The potential versus specific capacity plot at different cycles and different current regimes is shown in Figure 6, which clearly fits with the CV results and accounts for the typical electrochemical behavior of these mixed oxide systems in line with previous literature reports.^[47] In general, a very limited reduction in specific capacity was observed up to 5 mA g⁻¹ (>700 mAh g⁻¹ provided) and a considerable drop is documented only at very high current density as high as 10 mA g⁻¹ (i.e., 1280 mA considering the effective area active material loading in the electrode disk); nonetheless, at such a very high current density the cell still delivered more than

400 mAh g⁻¹. It accounts for an impressive rate capability (see also the rate capability plot in Figure 4b), which is a fundamental parameter when materials for high power devices are envisaged. Interestingly, at high rates some capacitive contribution from the graphene nanosheets was also observed, which may have positively contributed to the stability of the active material particles. To get a better insight into the enhanced performance, the differential capacity was investigated at different cycles (i.e., 1, 50, 100, 200, 300, 400, and 500 cycles). The corresponding dQ dV⁻¹ versus V plot is shown in the Supporting Information (Figure S4, Supporting Information). The results agree with the CV profiles shown in Figure 4a, confirming also a similar evolution of the electrode upon cycling. The dQ dV⁻¹ profiles for the succeeding cycles are different from the initial ones, which confirms severe modifications in the oxide microstructures upon reversible reaction with lithium ions. The trend of enhanced electrochemical performance and material activation after initial modifications is well evidenced by the gradual increase of the intensity of the respective peaks, which also recover their shape upon prolonged cycling. The electrochemical processes in the dQ dV⁻¹ profiles overlap with subsequent cycles (>100 cycles), indicating good stability and reversibility after the initial cycling in which the material is gradually activated.^[54] Indeed, during prolonged cycling, no significant peak shifts toward lower potential (lithiation curve) and higher potential (delithiation curve) are observed, which is consistent with an almost negligible enhanced cell impedance due to the positive effect of graphene.^[55]

From a practical viewpoint, a potential window of around 3 V for an electrode can affect the final energy density of a full cell system. However, at low current rates, the maximum capacity is delivered below 1.5 V versus Li. In our opinion, such systems can be coupled with high working voltage cathodes, as it helps to reduce the overall potential of the cell, diminishing the detrimental effects of high voltage on the commonly used electrolytes.

A direct confirmation of the mechanical stability and the effectively retained morphological features of the CNO@GNS nanocomposite microsphere electrode material was obtained by ex situ SEM and TEM analyses after cycling. The SEM and TEM images of the CNO@GNS electrode after 500 reversible charge/discharge cycles are shown in Figures 2f and 3d, respectively. Although the mesoporous characteristics of the nanocast particles and the assembled microsphere morphology are hardly detectable in the SEM image, also due to the presence of the conducting agent and CMC binder in the electrode and the electrolyte residuals that remained even after thorough washing, the nanostructured CNO particles fairly retained their overall integrity upon repetitive cycling (Figure 3d). Some denser nanocrystals can nevertheless be observed along with preserved mesostructured particles. The CNO particles are clearly wrapped by the GNS network, which confirms its fundamental role in stabilizing the behavior of the mixed oxide by effectively limiting the electrochemically driven diffusion limitations induced upon conversion reaction into the nanocast particles. A confirmation of this as well as further evidence of the stability of the CNO@GNS nanocomposite microspheres upon long-term reversible cycling was obtained by electrochemical impedance spectroscopy (EIS)

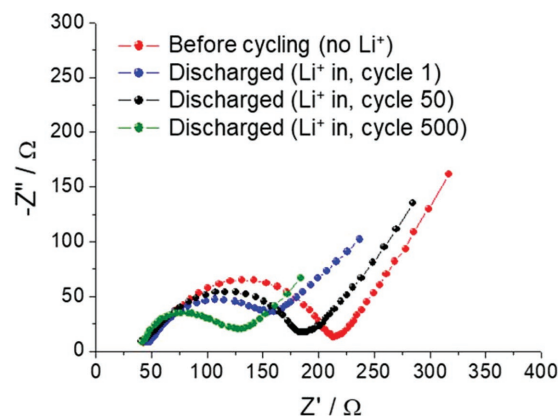


Figure 7. Nyquist plots for the CNO@GNS nanocomposite microsphere electrode before and after consecutive reversible charge/discharge cycles (up to 500) in lab-scale lithium cell.

measurements. Nyquist plots shown in Figure 7 have an intercept at high frequency (R_b , bulk resistance, used to evaluate the electronic conductivity), followed by a depressed semicircle in the intermediate frequency region (R_{ct} , charge transfer resistance indicating the diffusion capability of the lithium ions at the electrode/electrolyte interface), and a slope line in the low-frequency range (Warburg resistance, indicating the diffusion rate of lithium ions in the active electrode material).^[56,57] In the present case, R_b does not significantly change while cycling, which indicates a steady electronic conductivity of the material upon cycling due to the presence of GNS; moreover, R_{ct} constantly decreases, thus indicating an enhanced diffusion of the lithium ions in the active material particles, which also ameliorates during operation, and corroborating the previously discussed results.

As mentioned before, very long-term cycling data have been plotted in Figure 5, where the specific capacity versus number of cycles is shown along with four different graphs where the specific capacity versus number of cycles is also shown at different cycles, also including the capacity retention percentage normalized over the highest specific capacity value obtained after 800 cycles (viz. 871 mAh g⁻¹). It allows us to highlight the outstanding stability of the CNO@GNS nanocomposite microspheres upon extremely long-term cycling exceeding 3000 consecutive charge/discharge cycles, even at very high current density, with a capacity retention approaching 50% at very high current density of 10 mA g⁻¹ as well as exceeding 55% (at 1 mA g⁻¹) after more than 3000 consecutive cycles. To our knowledge, it is among the best performances reported so far in the literature for a conversion reaction metal oxide system (see Table S1 in the Supporting Information comparing the most relevant parameters of the recent literature reports).

3. Conclusion

In conclusion, a one-pot spray drying procedure has been successfully employed for the preparation of mixed metal oxide-based@graphene electrode active material, which can be used as superior alternative anode in the next generation of high-performing and long-lasting Li-ion batteries. The material is

made of 3D mesoporous binary copper-nickel oxide nanocast particles tightly wrapped by exfoliated graphene sheets, forming a caged system of 3D/2D mesoporous nanocomposite microspheres. Owing to the synergistic stabilization effect of the 2D exfoliated graphene sheets on mixed TMOs and the peculiar preparation procedure, the resulting nanocomposite exhibits unpredicted properties and functionalities that are not just the sum of individual components but rather a new active electrode material. Engineering void space in transition metal oxide nanostructures can address the problem of volumetric expansion and the anchoring of the transition metal oxide particles on the graphene sheets favors long-term cycling stability even at higher current regimes, as demonstrated by TEM and EIS postcycling analysis. Indeed, the presence of graphene sheets tightly wrapping the active material particles significantly improves their electronic conductivity, which strongly limits diffusion-driven phenomena and severe particle aggregation/pulverization upon reversible conversion reaction in real cell configuration. As a result, the newly elaborated porous CNO@GNS 3D/2D nanocomposite microspheres show outstanding electrochemical performances, i.e., a significantly improved specific capacity with unprecedented reversible cycling stability exceeding 3000 charge/discharge cycles at 100% DoD even at very high current regimes (up to effective 1280 mA) as compared to the pristine mixed oxide. To the best of our knowledge, such an extremely long-term cycling stability was never obtained for a mixed metal oxide-based electrode with such a low content of carbonaceous substrates (<5% including the graphene conductive wrapping agent and carbon black additive). Despite the huge number of research articles focused on lithium-ion battery anodes, here we presented a cheap, rapid, and reliable preparation procedure of CNO@GNS nanocomposite Li-ion battery anodes showing outstanding high and durable performance in real cell configuration, which originates from their superior characteristics compared to those of most transition metal oxide nanostructures and composites reported in the literature. This work further opens up new opportunities for exploring preferable strategies to develop efficient and durable TMO@GNS nanocomposite anode materials for advanced LiBs or other energy storage devices.

4. Experimental Section

Materials and Preparation Procedures: Unless otherwise stated, chemicals were purchased from Sigma-Aldrich and used as received. First, mesoporous mixed CuO-NiO nanoparticles were synthesized following a previously reported single-step nanocasting method using mesoporous silica as solid template.^[22,58] Briefly, 3 g of metal nitrate salt precursors was ground in the desired molar ratio of 1:2 Cu/Ni. This ratio was selected since our previous work showed that a ratio of 1:1 of Cu/Ni resulted in a high quantity of segregated phase of CuO, while a lower Cu/Ni ratio led to a more uniform insertion of Cu in the NiO matrix, as a solid solution.^[22] The 1:2 ratio was considered optimal, with a balance composition of some segregated CuO and Cu₂Ni₃O phases (see XRD analysis), which led to better performance in LiBs. After which, 1 g of mesoporous KIT-6 silica template^[59] was added to the preground precursor powder and further mixed in an agate mortar in the presence of cyclohexane. Once the mixture was homogenous, the slurry was dispersed in 30 mL of cyclohexane and refluxed at 85 °C for at least 20 h. After filtration, the sample was dried at 45 °C overnight, and then

calcined at 400 °C (1 °C min⁻¹) for 5 h. Finally, the silica template was removed by soaking in 0.7 M of NaOH at ambient temperature for 24 h. The removal procedure was repeated three times. The obtained mixed Cu/Ni metal oxide sample is referred to as CNO.

For the preparation of the mixed Cu/Ni metal oxide@graphene (namely CNO@GNS) nanocomposite microspheres, reduced graphene (obtained from Graphite Kropfmühl, Germany) was exfoliated into deionized water by ultrasonication (power 150 W, pulse cycles of 10 s on/off for 20 min) to form a suspension of graphene sheets with a concentration of 1 mg mL⁻¹. Thereafter, the CNO powder was added into the suspension in the 15:1 weight ratio of CNO:GNS. The mixture was ultrasonicated for 1 h and, subsequently, spray-dried to form the mixed CNO@GNS nanocomposite microspheres by means of a Buchi B-290 Mini spray dryer (BUCHI, Swiss). The heater inlet and outlet temperatures were held constant at 220 and 125 °C, respectively. The aspirator ran at a maximum air speed of 40 m³ h⁻¹. The feeding speed was kept constant at 5.1 mL min⁻¹ and the N₂ gas flow was set at 670 L h⁻¹. The product was collected at the vessel and, subsequently, treated in an inert atmosphere of Ar flow at 300 °C for 2 h to achieve the reduction of graphene that eventually underwent partial oxidation upon preparation of the CNO@GNS nanocomposite. The resulting nanocomposite was used for the fabrication of the electrodes without any further treatment.

Structural/Morphological Characterization: The wide-angle XRD patterns were collected on a Siemens D5000 (Cu K α : λ = 1.541 Å; 40 kV; 30 mA; 30°–50° 2 θ , step size: 0.02° 2 θ ; 0.02 s per step). The Jade (v 2.1) software coupled with JCPDS and ICDD (2001 version) databases was used to analyze the XRD data. The low angle XRD patterns were obtained with a Rigaku Multiflex diffractometer using Cu K α radiation at 40 mA and 30 kV. The XRD scanning was performed at steps of 0.02° with an accumulation time of 2 s. The N₂ adsorption-desorption isotherms were obtained at -196 °C with an Autosorb-1-MP sorption analyzer (Quantachrome Instruments, Boynton Beach, Florida, USA). Samples were outgassed at 150 °C for 12 h before analysis. The surface area (S_{BET}) was determined using the Brunauer-Emmett-Teller equation in the pressure range of $0.05 \leq P/P_0 \leq 0.20$ and the total pore volume (V_{pore}) was measured at $P/P_0 = 0.95$. Pore size distribution was calculated from the adsorption isotherm branch using NLDFT methods considering a cylindrical-pore geometry. High resolution scanning electron microscopy was carried out on a Verios 460 (FEI) at landing voltage of 5 kV in deceleration mode (stage bias voltage: 4 kV). Samples were mounted on an aluminum holder using carbon tape without crushing or metal coating (KAIST, Daejeon, Republic of Korea). TEM images were captured using a Titan G2 ETM at an accelerating voltage of 300 kV. Before the analysis, all samples were dispersed in acetone for 5 min through ultrasonication. The solution was dropped onto a carbon-coated copper grid and dried under vacuum for 1 h at 60 °C. Energy dispersive spectra were recorded with a ZEISS MERLIN instrument equipped with an EDS detector (OXFORD). A PHI 5000 Versaprobe II Scanning X-ray Photoelectron Spectrometer, equipped with a monochromatic Al K-alpha X-ray source (1486.6 eV energy, 15 kV voltage, and 1 mA anode current), was used to investigate surface chemical composition. A spot size of 100 μm was used in order to collect the photoelectron signal for both the high resolution (HR) and the survey spectra. Different pass energy values were exploited: 187.85 eV for survey spectra and 23.5 eV for HR peaks.

Electrode Preparation, Cell Assembly, and Electrochemical Testing: The electrodes for the evaluation of the electrochemical behavior were prepared by fully water-based spray-assisted procedure, exploiting the sodium salt of carboxymethylcellulose (Na-CMC, average M_n : 250 000) as binder. Initially, Na-CMC was dissolved in doubly deionized water followed by the addition of carbon black as electronic conductivity enhancer (Super P, MMM Carbon Belgium) and the CNO@GNS active material particles under continuous stirring (\approx 3 h). The obtained slurry was then spray-coated on a copper current collector film. Resulting electrode films were dried under fume hood at ambient conditions. Then, disks of 2.54 cm² were cut from the foil and heat-treated under high vacuum overnight at 130 °C. Then, the electrode disks were transferred into an

Ar-filled dry glove box (MBraun Labstar, O₂ and H₂O content <1 ppm). The composition of the electrodes was 95:1:4 wt% in CNO@GNS, Super P, and Na-CMC, respectively. The effective areal active material loading was about 7.8 mg cm⁻². Composite electrodes were assembled in three electrode electrochemical test cells with a reference electrode (model ECC-Ref test cells, EL-CELL GmbH, <http://el-cell.com/products/test-cells/ecc-ref>) where lithium metal acts as the counter electrode (also as the reference electrode in the case of cyclic voltammetry), CNO@GNS-based composite electrode as the working electrode and a glass wool (Whatman GF/A) disc as the separator. The liquid electrolyte (<100 μL) used for lithium test cell assembly was a 1 M solution of LiPF₆ in a 1:1 mixture of ethylene carbonate and dimethyl carbonate. Battery grade electrolyte components were purchased from Solvionic (France), and then prepared in the form of solution at the required compositions. The evaluation of the electrochemical performances was carried out at ambient temperature by cyclic voltammetry (between 0.02 and 3.0 V vs Li⁺/Li, scan rate of 0.100 mV s⁻¹) and constant current (galvanostatic) charge/discharge cycling (cut off potentials: 0.02–3.0 V vs Li⁺/Li, various current rates from 0.1 to 10 mA g⁻¹, viz. 12.8 to 1280 mA as for the effective areal active material loading in the electrode disk), on an Arbin Instrument Testing System model BT-2000 instrument. Note that, charge refers to lithium de-insertion (de-alloying) while discharge to lithium insertion (alloying). Charge/discharge cycles were set at the same rate at different current densities. Clean electrodes and fresh samples were used for each test. To confirm the results obtained, the tests were performed at least twice on different fresh samples. All the procedures of cell assembly, electrolyte preparation, and related activities were performed in the inert atmosphere of the dry glove box.

Supporting Information

Supporting Information is available from the Wiley Online Library or from the author.

Acknowledgements

L.L.P. and F.C. contributed equally to this work. L.L.P. and F.K. acknowledge financial support from the Natural Sciences and Engineering Research Council (Canada) and Fonds Québécois de la Recherche sur la Nature et les Technologies (Quebec). J.F. and F.K. thank the funding support of the University of Vienna (Austria). The authors thank Prof. R. Ryoo (KAIST, Daejeon, Korea) for the access to high-resolution TEM and SEM microscopes. L.L.P. and F.K. thank the Gouvernement du Québec, Ministère des Relations internationales et de la Francophonie and the consulat général d'Italie à Montréal for funding in the exchange program “VIII^e réunion de la sous-commission mixte de Québec-Italie (coopération 2013–2015)”. C.G., F.B., and G.M. acknowledge funding from the Italian government as part of this work was carried out within the activities “Ricerca Sistema Elettrico” funded through contributions to research and development by the Italian Ministry of Economic Development.

Conflict of Interest

The authors declare no conflict of interest.

Keywords

graphene, lithium batteries, mesoporous mixed oxides, nanocast nickel-copper anode, spray drying

Received: August 6, 2018
Revised: September 21, 2018
Published online: October 31, 2018

- [1] a) M. Armand, J.-M. Tarascon, *Nature* **2008**, *451*, 652; b) G. E. Blomgren, *J. Electrochem. Soc.* **2017**, *164*, A5019; c) A. Manthiram, *ACS Cent. Sci.* **2017**, *3*, 1063; d) P. G. Bruce, B. Scrosati, J.-M. Tarascon, *Angew. Chem., Int. Ed.* **2008**, *47*, 2930; e) J.-M. Tarascon, *Philos. Trans. R. Soc., A* **2010**, *368*, 3227; f) B. Scrosati, *J. Solid State Electrochem.* **2011**, *15*, 1623.
- [2] Y. Wang, B. Liu, Q. Li, S. Cartmell, S. Ferrara, Z. D. Deng, J. Xiao, *J. Power Sources* **2015**, *286*, 330.
- [3] www.gminsights.com/industry-analysis/lithium-ion-battery-market (accessed: September 2018).
- [4] K. Amine, R. Kanno, Y. Tzeng, *MRS Bull.* **2014**, *39*, 395.
- [5] W. Ke, S. Zhang, X. He, Y. Wu, J. Hao, *Applied Energy* **2017**, *188*, 367.
- [6] P. Poizot, S. Laruelle, S. Grugeon, L. Dupont, J.-M. Tarascon, *Nature* **2000**, *407*, 496.
- [7] B. Scrosati, J. Garche, *J. Power Sources* **2010**, *195*, 2419.
- [8] J. B. Goodenough, K.-S. Park, *J. Am. Chem. Soc.* **2013**, *135*, 1167.
- [9] Q. Cheng, Y. Zhang, *J. Electrochem. Soc.* **2018**, *165*, A1104.
- [10] M.-S. Balogun, W. Qiu, Y. Luo, H. Meng, W. Mai, A. Onasanya, T. K. Olaniyi, Y. Tong, *Nano Res.* **2016**, *9*, 2823.
- [11] M. Valvo, D. Rehnlund, U. Lafont, M. Hahlin, K. Edström, L. Nyholm, *J. Mater. Chem. A* **2014**, *2*, 9574.
- [12] X. Zhang, J. Zhou, H. Song, X. Chen, Y. V. Fedoseeva, A. V. Okotrub, L. G. Bulusheva, *ACS Appl. Mater. Interfaces* **2014**, *6*, 17236.
- [13] H. Liu, G. Wang, J. Liu, S. Qiao, H. Ahn, *J. Mater. Chem.* **2011**, *21*, 3046.
- [14] S. Sun, Y. Nie, M. Sun, T. Liang, M. Sun, H. Yang, *Mater. Lett.* **2016**, *176*, 87.
- [15] B. D. Polat, O. Keles, *J. Alloys Compd.* **2016**, *677*, 228.
- [16] X. H. Huang, P. Zhang, J. B. Wu, Y. Lin, R. Q. Guo, *Mater. Res. Bull.* **2016**, *80*, 30.
- [17] C. Lv, X. Yang, A. Umar, Y. Xia, Y. Jia, L. Shang, T. Zhang, D. Yang, *J. Mater. Chem. A* **2015**, *3*, 22708.
- [18] J. Yu, S. Chen, W. Hao, S. Zhang, *ACS Nano* **2016**, *10*, 2500.
- [19] J.-M. Tarascon, M. Armand, *Nature* **2001**, *414*, 359.
- [20] X. H. Huang, J. P. Tu, C. Q. Zhang, J. Y. Xiang, *Electrochem. Commun.* **2007**, *9*, 1180.
- [21] Z. Sun, E. Madej, C. Wiktor, I. Sinev, R. A. Fischer, G. van Tendeloo, M. Muhler, W. Schuhmann, E. Ventosa, *Chem. - Eur. J.* **2015**, *21*, 16154.
- [22] H. Yen, F. Kleitz, *J. Mater. Chem. A* **2013**, *1*, 14790.
- [23] A.-H. Lu, F. Schüth, *Adv. Mater.* **2006**, *18*, 1793.
- [24] M. Tiemann, *Chem. Mater.* **2008**, *20*, 961.
- [25] F. Jiao, K. M. Shaju, P. G. Bruce, *Angew. Chem., Int. Ed.* **2005**, *44*, 6550.
- [26] F. Jiao, A. Harrison, J.-C. Jumas, A. V. Chadwick, W. Kockelmann, P. G. Bruce, *J. Am. Chem. Soc.* **2006**, *128*, 5468.
- [27] F. Jiao, A. Harrison, A. H. Hill, P. G. Bruce, *Adv. Mater.* **2007**, *19*, 4063.
- [28] a) F. Jiao, H. Yen, G. S. Hutchings, B. Yonemoto, Q. Lu, F. Kleitz, *J. Mater. Chem. A* **2014**, *2*, 3065; b) C. Yuan, H. B. Wu, Y. Xie, X. W. Lou, *Angew. Chem., Int. Ed.* **2014**, *53*, 1488.
- [29] C. Wang, Q. Li, F. Wang, G. Xia, R. Liu, D. Li, N. Li, J. S. Spendelov, G. Wu, *ACS Appl. Mater. Interfaces* **2014**, *6*, 1243.
- [30] Z. Zhang, H. Che, J. Sun, X. She, H. Chen, F. Su, *J. Nanosci. Nanotechnol.* **2013**, *13*, 1530.
- [31] Y. Ren, Z. Ma, R. E. Morris, Z. Liu, F. Jiao, S. Dai, P. G. Bruce, *Nat. Commun.* **2013**, *4*, 2015.
- [32] F. Jiao, P. G. Bruce, *Adv. Mater.* **2007**, *19*, 657.
- [33] G.-N. Zhu, H.-J. Liu, J.-H. Zhuang, C.-X. Wang, Y.-G. Wang, Y.-Y. Xia, *Energy Environ. Sci.* **2011**, *4*, 4016.
- [34] H. Li, Y. Li, Y. Zhang, C. Zhang, *J. Nanopart. Res.* **2015**, *370*, 1.
- [35] B. Mohamed, V. Malgras, T. Takei, L. Cuiling, Y. Yamauchi, *Chem. Commun.* **2015**, *51*, 16409.
- [36] L. Pan, X.-D. Zhu, X.-M. Xie, Y.-T. Liu, *Adv. Funct. Mater.* **2015**, *25*, 3341.

- [37] a) G. Zhou, D.-W. Wang, L.-C. Yin, N. Li, F. Li, H.-M. Cheng, *ACS Nano* **2012**, *6*, 3214; b) Y. J. Mai, X. L. Wang, J. Y. Xiang, Y. Q. Qiao, D. Zhang, C. D. Gu, J. P. Tu, *Electrochim. Acta* **2011**, *56*, 2306; c) X. Xin, X. Zhou, J. Wu, X. Yao, Z. Liu, *ACS Nano* **2012**, *6*, 11035.
- [38] M. Ren, M. Yang, W. Liu, M. Li, L. Su, C. Qiao, X. Wu, H. Ma, *Electrochim. Acta* **2016**, *194*, 219.
- [39] a) Z.-S. Wu, W. Ren, L. Wen, L. Gao, J. Zhao, Z. Chen, G. Zhou, F. Li, H.-M. Cheng, *ACS Nano* **2010**, *4*, 3187; b) S. Xiao, D. Pan, L. Wang, Z. Zhang, Z. Lyu, W. Dong, X. Chen, D. Zhang, W. Chen, H. Li, *Nanoscale* **2016**, *8*, 19343; c) H. Wang, C. Guan, X. Wang, H. J. Fan, *Small* **2015**, *11*, 1470; d) W. Zheng, Z. Yan, Y. Dai, N. Du, X. Jiang, H. Dai, X. Li, G. He, *ACS Appl. Mater. Interfaces* **2017**, *9*, 20491.
- [40] Q. Zhang, H. Chen, X. Han, J. Cai, Y. Yang, M. Liu, K. Zhang, *ChemSusChem* **2016**, *9*, 186.
- [41] B. Wang, M.-Q. Yang, N. Zhang, Y.-J. Xu, *J. Mater. Chem. A* **2014**, *2*, 9380.
- [42] a) H. Yen, Y. Seo, S. Kaliaguine, F. Kleitz, *Angew. Chem., Int. Ed.* **2012**, *51*, 12032; b) X. Lai, X. Li, W. Geng, J. Tu, J. Li, S. Qiu, *Angew. Chem., Int. Ed.* **2007**, *46*, 738.
- [43] G. Longoni, R. L. Pena Cabrera, S. Polizzi, M. D'Arienzo, C. M. Mari, Y. Cui, R. Ruffo, *Nano Lett.* **2017**, *17*, 992.
- [44] Y. Sun, G. Ji, M. Zheng, X. Chang, S. Li, Y. Zhang, *J. Mater. Chem.* **2010**, *20*, 945.
- [45] A. Ruplecker, F. Kleitz, E.-L. Salabas, F. Schüth, *Chem. Mater.* **2007**, *19*, 485.
- [46] X. Wang, G. Wang, G. Zhai, H. Wang, *Aust. J. Chem.* **2015**, *68*, 964.
- [47] W. Guo, W. Sun, Y. Wang, *ACS Nano* **2015**, *9*, 11462.
- [48] X. Wang, Z. Yang, X. Sun, X. Li, D. Wang, P. Wang, D. He, *J. Mater. Chem.* **2011**, *21*, 9988.
- [49] C. Wang, D. Higgins, F. Wang, D. Li, R. Liu, G. Xia, N. Li, Q. Li, H. Xu, G. Wu, *Nano Energy* **2014**, *9*, 334.
- [50] Z.-L. Hu, H. Chen, C.-L. Li, N. Li, K.-X. Xiang, *Micro Nano Lett.* **2013**, *8*, 544.
- [51] X. Chen, N. Zhang, K. Sun, *J. Mater. Chem.* **2012**, *22*, 13637.
- [52] J. Zhang, M. Zhang, L. Zhang, *Electrochim. Acta* **2013**, *105*, 282.
- [53] M. Yang, Q. Gao, *Microporous Mesoporous Mater.* **2011**, *143*, 230.
- [54] S. H. Nam, Y. S. Kim, H.-S. Shim, J. G. Kim, W. B. Kim, *Nanoscale Res. Lett.* **2011**, *6*, 292.
- [55] C. Ma, J. Xu, J. Alvarado, B. Qu, J. Somerville, J. Y. Lee, Y. S. Meng, *Chem. Mater.* **2015**, *27*, 5633.
- [56] F. Bella, A. B. Muñoz-García, G. Meligrana, A. Lamberti, M. Destro, M. Pavone, C. Gerbaldi, *Nano Res.* **2017**, *10*, 2891.
- [57] T. Anwar, L. Wang, R. U. R. Sagar, F. Nosheen, R. Singh, H. M. Jafri, K. Shehzad, T. X. Liang, *J. Mater. Sci.* **2017**, *52*, 4323.
- [58] H. Yen, Y. Seo, R. Guillet-Nicolas, S. Kaliaguine, F. Kleitz, *Chem. Commun.* **2011**, *47*, 10473.
- [59] a) F. Kleitz, S. H. Choi, R. Ryoo, *Chem. Commun.* **2003**, 2136; b) J. Florek, F. Chalifour, F. Bilodeau, D. Larivière, F. Kleitz, *Adv. Funct. Mater.* **2014**, *24*, 2668.